

Resistive memory-based zero-shot liquid state machine for multimodal event data learning

Ning Lin^{1,2,3,†}, Shaocong Wang^{1,2,3,†}, Yi Li^{1,2,4,†}, Bo Wang^{1,3}, Shuhui Shi^{1,3}, Yangu He^{1,3}, Woyu Zhang^{2,4}, Yifei Yu^{1,3}, Yue Zhang^{1,3}, Xiaojuan Qi¹, Xiaoming Chen⁷, Hao Jiang⁵, Xumeng Zhang⁵, Peng Lin⁶, Xiaoxin Xu^{2,4}, Qi Liu^{2,5}, Zhongrui Wang^{1,2,*}, Dashan Shang^{2,4,*}, and Ming Liu^{2,5}

¹Department of Electrical and Electronic Engineering, the University of Hong Kong, Hong Kong, China

²State key Lab of Fabrication Technologies for Integrated Circuits, Institute of Microelectronics, Chinese Academy of Sciences, Beijing 100029, China

³ACCESS – AI Chip Center for Emerging Smart Systems, InnoHK Centers, Hong Kong Science Park, Hong Kong, China

⁴University of Chinese Academy of Sciences, Beijing 100049, China

⁵Frontier Institute of Chip and System, Fudan University, Shanghai 200433, China

⁶College of Computer Science and Technology, Zhejiang University, Zhejiang 310027, China

⁷Institute of Computing Technology, Chinese Academy of Sciences, Beijing 100190, China

[†]These authors contributed equally.

*e-mail: zrwang@eee.hku.hk; shangdashan@ime.ac.cn

ABSTRACT

The human brain is a complex spiking neural network (SNN) that learns multimodal signals in a zero-shot manner by generalizing existing knowledge. Remarkably, the brain achieves this with minimal power consumption, using event-based signals that propagate within its structure. However, mimicking the human brain in neuromorphic hardware presents both hardware and software challenges. Hardware limitations, such as the slowdown of Moore’s law and the von Neumann bottleneck, hinder the efficiency of digital computers. On the software side, SNNs are known for their difficult training, especially when learning multimodal signals. To overcome these challenges, we propose a hardware-software co-design that combines a fixed and random liquid state machine (LSM) SNN encoder with trainable artificial neural network (ANN) projections. The LSM is physically implemented using analogue resistive memory, leveraging the inherent stochasticity of resistive switching to generate random weights. This highly efficient and nanoscale in-memory computing approach effectively addresses the von Neumann bottleneck and the slowdown of Moore’s law. The ANN projections are implemented digitally, allowing for easy optimization using contrastive loss, which helps to overcome the difficulties associated with SNN training. We experimentally implement this co-design on a 40nm 256Kb in-memory computing macro. We first demonstrate LSM-based event encoding through supervised classification and linear probing on the N-MNIST and N-TIDIGITS datasets. Based on that, we showcase the zero-shot learning of multimodal event data on our co-design, achieving classification accuracy comparable to fully optimized software models. This not only results in a 152.83-fold reduction in training costs compared to state-of-the-art contrastive language-image pre-training (CLIP) and Prototypical networks, but also delivers a 23.34-fold improvement in energy efficiency compared to cutting-edge digital hardware. These proof-of-principle prototypes not only demonstrate the efficient and compact neuromorphic hardware using in-memory computing, but also zero-shot learning multimodal events in a brain-inspired manner, paving the way for future edge neuromorphic intelligence.

Introduction

The human brain is a highly efficient and adaptable system that effectively integrates and learns from diverse sensory inputs, often through the generalization of existing knowledge to new tasks. This so-called zero-shot transfer learning is incredibly energy-efficient and parallel, due to the coexistence of memory and computing within the extensively interconnected synapses and neurons, and the propagation of event-type spikes throughout the neural network¹⁻⁴.

Inspired by the human brain, neuromorphic hardware, including spiking neural network (SNN) accelerators and event-based dynamic vision and audio sensors⁵⁻¹⁰, aims to emulate the functionality of the brain and sensory neural networks, such as the retina and cochlea¹¹⁻¹³. Despite these efforts, achieving a level of energy efficiency and zero-shot crossmodal intelligence comparable to the human brain remains a considerable challenge. This is due to obstacles encountered in both hardware and software domains. Hardware-wise, transistor scaling is close to its physical limit, which has slowed down Moore’s law that has

driven the past development of complementary metal-oxide-semiconductor (CMOS) chips for decades. In addition, digital neuromorphic hardware faces the von Neumann bottleneck, characterized by frequent and massive data transfers between off-chip memory and processing units, resulting in large energy and time overheads^{1,4,14–26}.

From a software standpoint, training SNNs has historically been a challenging issue. The asynchronous and complex dynamics of spiking neurons are known for their non-differentiability. While surrogate gradients can approximate this non-differentiability at considerable training costs²⁷, the performance typically does not surpass that of training an artificial neural network (ANN) and mapping weights to the corresponding SNN. Besides, the latter^{28,29} is difficult to parallel the performance of original ANNs, due to the absence of neural dynamics in ANN training³⁰. Moreover, unsupervised local learning rules, such as spike-timing-dependent plasticity (STDP) practiced by biological synapses, have been found to be ineffective for deep SNNs^{31,32}. Furthermore, existing SNNs for event data predominantly depend on supervised learning with a large number of sample-label pairs, rather than capitalizing on pre-training and generalization from prior experiences to accomplish zero-shot transfer learning, a technique popularized by recent large-scale language and vision ANN models^{33,34}. As such, the challenges in both hardware and software necessitate a novel neuromorphic computing paradigm for learning crossmodal event-driven signals.

To address these challenges, we propose a hardware-software co-design that employs a hybrid analogue-digital system for a combined SNN-ANN model. On the hardware side, we develop a hybrid system that integrates analogue random resistive memory with a digital computer. The inherent stochasticity of resistive switching is harnessed to physically generate fixed, random and nanoscale resistors (resistive switches or memristors) and compute with simple physical laws. This method naturally overcomes the von Neumann bottleneck and achieves improved efficiency^{14,18,20–22,35–49}. Concurrently, the digital hardware enables fast and precise real-time learning. From a software perspective, the LSM⁵⁰ encoder is an SNN variant of reservoir computing that comprises fixed, random and recurrent synaptic connections, which can be naturally implemented on the analogue random resistive memory to directly process multimodal (e.g., visual and audio) event data. These spiking features are then accumulated as real-valued vectors and aligned by trainable ANN projection layers in a shared latent space using contrastive learning. This effectively brings matched visual-audio embedding pairs closer together while pushing non-matched embedding pairs apart⁵¹, addressing the SNN training difficulty and achieving zero-shot transfer learning. The synergistic combination of analogue random resistive memory, multimodal LSM encoders, and contrastive learning not only improves energy-area efficiency through in-memory computing but also leverages the intrinsic stochasticity of dielectric breakdown in generating random weights. This leads to the development of low-cost, nanoscale neuromorphic hardware capable of zero-shot learning for crossmodal event-driven data at substantially reduced learning complexity.

In this article, we physically implement our hardware-software co-design with a 40nm resistive computing-in-memory macro. We showcase the effectiveness of LSM encoders using linear probing on representative event datasets N-MNIST⁵² and N-TIDIGITS⁵³, followed by illustrating the zero-shot transfer capability of the co-design on the multimodal event dataset. We achieve classification performance on par with software models, while showing a 23.32-fold improvement in energy efficiency compared to state-of-the-art digital hardware. Moreover, thanks to the random projections in LSM, the backward pass complexity is reduced by about 152.83-fold compared to the state-of-the-art spiking recurrent neural network (SRNN)-based CLIP⁵¹ and Prototypical networks⁵⁴. Our hardware-software co-design not only introduces a high-efficiency, fast, and precise learning solution for future compact edge neuromorphic systems but also enables zero-shot learning of crossmodal events in a brain-inspired manner.

Hardware-Software Co-Design

Fig. 1 depicts the hardware-software co-design, which utilizes a hybrid analogue-digital system to physically implement the SNN-ANN model.

Software-wise, the SNN-ANN model primarily comprises a fixed and random multimodal LSM encoder and trainable projections, as illustrated in Fig. 1(a-b). The LSM encoder is an SNN with an input layer and a recurrent layer, both featuring biologically plausible leaky integrate-and-fire (LIF) neurons⁵⁵ to directly handle event data. These spiking neurons are randomly interconnected with fixed synaptic weights, which map inputs to a high-dimensional state space trajectory. This process generates diverse input signal representations, typically achieving greater linear separability when the trajectory is at the edge of chaos, also known as the "separation property" of LSM.

Two ANN projection layers are utilized to map the distinct modalities' features, extracted by the LSM encoders, to the same dimension and measure their cosine distance. The projection layers' weights are optimized according to the contrastive loss, which prompts the model to distinguish between positive pairs (i.e., matching image-audio pairs) and negative pairs (i.e., non-matching image-audio pairs). This is accomplished by maximizing the similarity between positive pairs and minimizing the similarity between negative pairs, drawing inspiration from the success of CLIP model^{51,56}.

Hardware-wise, the hybrid analogue-digital computing platform (see Fig. 1 and Table 5 in Supplementary Information for the system design) has an analogue core, the resistive memory-based in-memory computing macro (Fig. 1c). The macro consists of

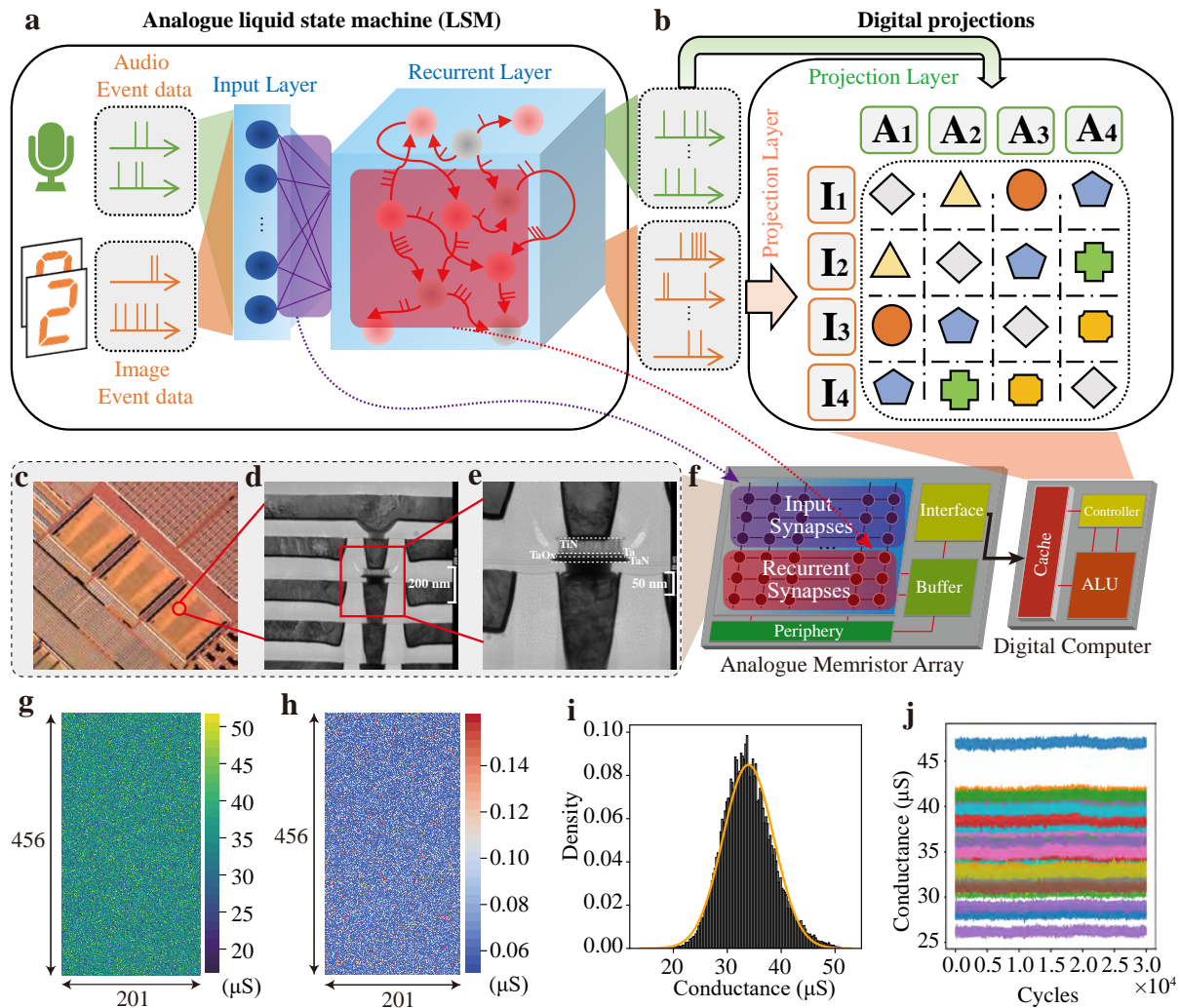


Figure 1. Hardware software co-design using the hybrid analogue-digital system for a combined LSM-ANN model. **a**, The liquid state machine (LSM) is a fixed, random and recurrent spiking neural network (SNN), which encodes multimodal event signals (e.g. images and sounds). The LSM is implemented using the analogue random resistive memory. **b**, The projection layers are trainable artificial neural network (ANN) layers that map accumulated spiking features from different modalities to real-valued feature vectors. The projection layers are implemented digitally and optimized by minimizing contrastive loss for zero-shot learning. **c**, Optical photo of the 40nm 256Kb resistive memory-based in-memory computing macro. **d**, A cross-sectional transmission electron micrograph shows the resistive memory crossbar array, fabricated by the backend-of-line process to integrate with complementary metal-oxide-semiconductor (CMOS). **e**, The cross-sectional transmission electron micrograph reveals a $TaN/TaO_x/Ta/TiN$ resistive memory cell, operating as a stochastic resistor subsequent to a post-dielectric breakdown. **f**, The schematic of the hybrid analogue-digital system. **g**, Conductance map of a 456×201 resistive memory subarray shared by two LSM encoders (456×201 and 264×201) for different modalities. (See Fig.2 in Supplementary Information for details.) **h**, Corresponding 30,000-cycle array conductance reading variance. **i**, The histogram of **g**. **j**, The cycle-to-cycle conductance of 40 randomly sampled resistive memory cells over 30,000 read cycles.

emerging nanoscale $TaN/TaO_x/Ta/TiN$ resistive switches (Fig.1d-e) integrated with CMOS using the backend-of-line process on a 40nm technology node tape-out, forming a 512×512 crossbar array. This analogue core implements both the input and recurrent layers of the LSM (Fig.1f), accounting for the majority of computational cost. The LSM is interfaced with ANN projection layers for contrastive learning that are implemented digitally.

The inherent stochasticity in resistive memory programming was harnessed to create random conductance matrices for representing synaptic weights in the LSM. Specifically, all as-deposited cells in a resistive memory array receive a uniform programming voltage, subject to current compliance enforced by selecting transistors to prevent hard breakdown. The resulting differential conductance map of a 456×201 subarray is depicted in Fig.1g. The random synaptic weights are partially shared

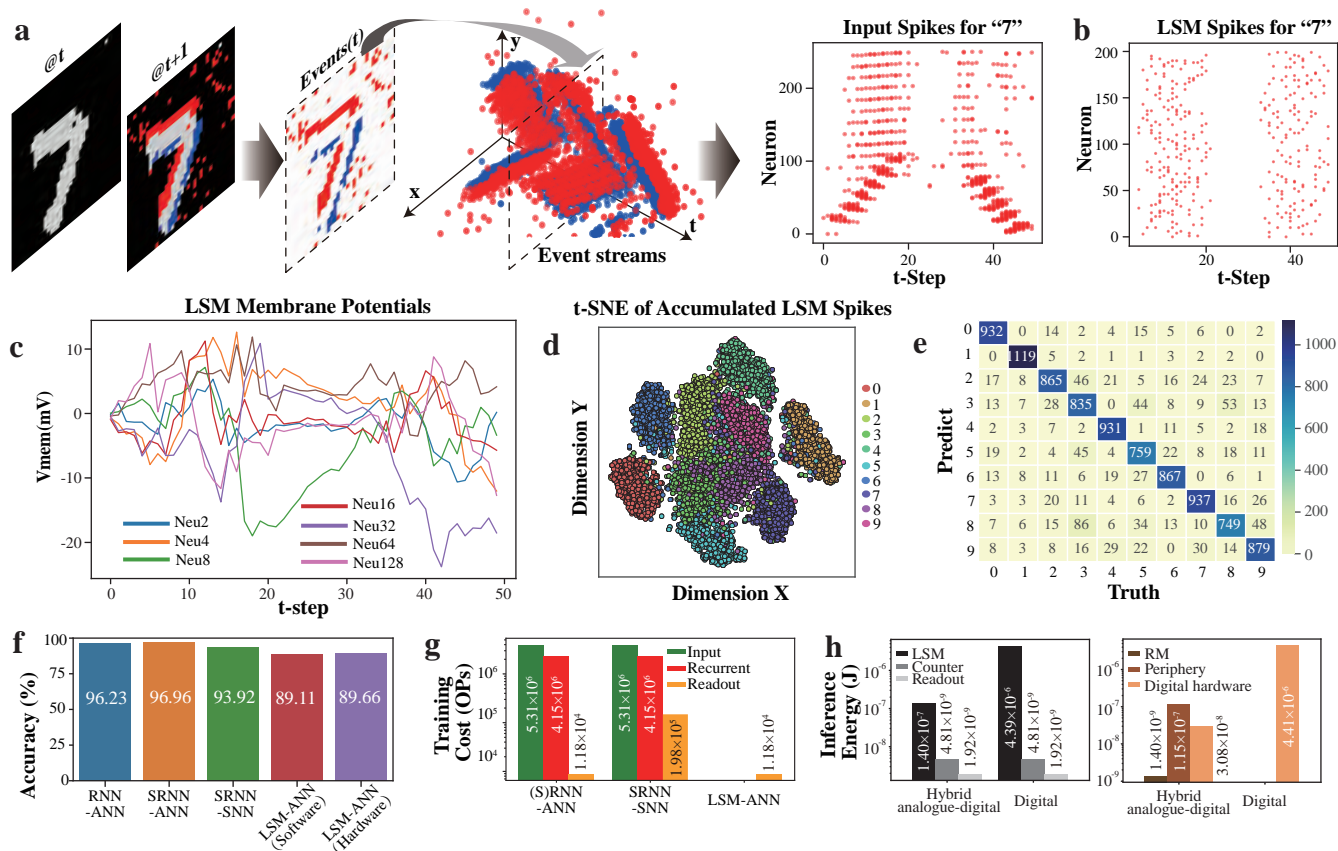


Figure 2. Event-based image classification with the N-MNIST dataset. **a**, Schematics of event-based image capture. Pixel changes between consecutive frames are encoded as events and input into the LSM encoder for spike number embedding, followed by a fully connected ANN classification layer. **b**, LSM hidden neuron spikes corresponding to the digit "7". **c**, Associated membrane potentials for selected neurons. **d**, Distribution of spike number embeddings for the test set, showing clear clustering. **e**, Confusion matrix of dominant diagonal elements. **f**, Accuracy comparison between experimental and simulated models (LSM-ANN), as well as fully trainable counterparts with SNN/ANN encoders/classifiers (RNN-ANN, SRNN-ANN, and SRNN-SNN), indicating a small performance gap. **g**, Breakdown of training complexity. The LSM exhibits a substantially lower training complexity compared to SRNN-SNN (by 817.95-fold) and SRNN-ANN (by 802.18-fold), highlighting a significant reduction in the training cost of the LSM. **h**, Breakdown of inference energy of the model across different hardware platforms. The hybrid analogue-digital system showcases a 29.91-fold reduction in energy consumption compared to state-of-the-art digital hardware, emphasizing the high efficiency of resistive memory (RM).

by the event-driven audio and image LSM encoders (refer to Fig.2 in Supplementary Information for details). Fig.1h shows the corresponding variance of 30,000-cycle array conductance reading. The reading variance for most devices remains below $0.14\mu\text{S}$, indicating decent data retention.

Fig.1i illustrates that the conductance of resistive memory cells follows a quasi-normal distribution, which can be tailored by adjusting electrical operation parameters, thus enabling flexible hardware implementations of the LSM-based backbone (see Fig.3 in Supplementary Information for the distribution of weights). The stability of such random resistive memory is highlighted by the repeated reading of 40 randomly selected cells within the resistive memory, as shown in Fig.1j.

Supervised N-MNIST Classification

First, we evaluate the performance of the LSM encoder using a supervised learning task on the N-MNIST dataset⁵² (see Table 2 in Supplementary Information for details of the dataset), which consists of spiking versions of handwritten digits represented by positive and negative events. First, we center crop the 34×34 frames to 16×16 frames, as illustrated by the events for digit "7" in Fig.2a. This represents the asynchronous and sparse spike stream fed to the LSM encoder at various time steps. The LSM encoder maps the input spike stream to the spike trains of a large population of recurrent neurons as shown in Fig.2b. Due to the near-chaotic dynamics, the event stream becomes more linearly separable. Fig.2c visualizes the

membrane potentials of selected LSM neurons upon the input spike stream, resulting from the synergy of both excitatory and inhibitory synaptic connections. LSM neuron spikes are aggregated by digital counters and interfaced with a downstream ANN classification head implemented digitally. Fig.2d displays the distribution of spiking number embedding of test samples using t-distributed stochastic neighbor embedding (t-SNE) for dimensionality reduction, demonstrating discriminability for most input classes due to LSM's separability. This is further evident in the confusion matrix shown in Fig.2e, which is characterized by dominant diagonal elements and high class-wise classification accuracy. Fig.2f presents the comparison study, where the hardware classification accuracy (89.66% with the LSM encoder and ANN classification head, or LSM-ANN) is close to the software simulation (89.11%). Additionally, Fig.2f shows that the model's performance is comparable to the fully trainable counterparts in software, such as those with spiking/non-spiking recurrent neural network (SRNN/RNN) encoders and ANN/SNN classification heads (see Notes 3-1 and 3-2 in Supplementary Information for the details of SRNN and RNN). Moreover, LSM's performance scales well with the hidden dimension and the input size, and is robust to noise disturbance (refer to Fig.4 in Supplementary Information for the hyperparameter impact, Fig.6 in Supplementary Information for noise impact).

To demonstrate the advantages of LSM over training complexity, we count the multiply-accumulate (MAC) operations of different layers of the model during training, as shown in Fig.2g. The LSM's training complexity is considerably lower than that of SRNN-SNN (by a factor of 817.95) and SRNN-ANN (by a factor of 802.18) primarily due to the fixed and random weights of the LSM encoder. Additionally, the training cost of the ANN classification head is lower than that of the SNN one, mainly because a simple accumulator is used for the SNN-ANN interface. The corresponding energy estimations are depicted in the two panels of Fig.2h. The overall energy consumption is estimated to be around $4.4\mu\text{J}$ for a conventional digital system and approximately $0.14\mu\text{J}$ for a projected hybrid analogue-digital system using 40nm technology node. The breakdown of energy consumption for different layers is depicted in the left panel. It is observed that the energy consumption of the conventional digital system is mainly attributed to the LSM, accounting for approximately $4.39\mu\text{J}$, which is 31.29-fold that of the hybrid analogue-digital system. Right panel shows the energy consumption of analogue and digital circuits. Overall, our hybrid analogue-digital system demonstrates a 29.91-fold improvement in energy consumption compared to the state-of-the-art digital hardware (see Table 6 in Supplementary Information for the detailed energy breakdown), thanks to the energy efficient resistive in-memory computing.

Supervised N-TIDIGITS Classification

In addition to event-based vision tasks, we also evaluate the performance of the LSM encoder on a representative audio classification problem using the N-TIDIGITS dataset⁵³ (see Table 2 in Supplementary Information for details). This dataset consists of audio recordings of spoken digits, which are represented by events across 64 frequency bands, as shown in Fig.3a. For simplicity, each sample is divided into 129 time steps and input into the LSM encoder, as illustrated in Fig.3b. The LSM encoder then outputs a high-dimensional event stream, which is more linearly separable, as depicted in Fig.3c. The membrane potentials of selected LSM neurons are displayed in Fig.3d, exhibiting different trajectories and thus spiking patterns between neurons.

The 3D visualization of the distribution of spike number embeddings of test samples, using t-SNE for dimensionality reduction, is presented in Fig.3e. Samples from the same category are clearly clustered, resulting from the nonlinear dynamics of LSM. Fig.3f shows the experimental confusion matrix, which, similar to the previous case, is dominated by diagonal elements, confirming high classification accuracy. The comparison study in Fig.3g shows the hardware and software classification accuracy (70.11% and 70.79%), as well as the performance of SRNN/RNN encoders with SNN/ANN classifiers, which are close. Also, LSM's performance, like in the previous case, is robust to both input noise and read noise, while scales with the hidden dimension (refer to Fig. 6 in Supplementary Information for noise impact simulation and Fig.5 in Supplementary Information for hyperparameter analysis).

Fig.3h displays the training-related MAC operations for different layers of the model. Similar to the previous case, LSM's training complexity, with about 13K operations, is significantly lower than that of SRNN-SNN (by a factor of 1102.92) and SRNN-ANN (by a factor of 1061.60). This is due to the fixed random weights of the LSM encoder and the use of simple accumulators for the LSM-ANN interface. Fig.3i compares the inference energy consumption across various hardware platforms, including a projected hybrid analogue-digital system on 40nm technology node and the latest digital hardware (refer to Table 7 in Supplementary Information for the detailed energy breakdown). Notably, the estimated inference energy for the digit "7" on the hybrid analogue-digital system is $0.37\mu\text{J}$, which is about 22.07-fold smaller compared to a fully digital implementation. This is because resistive in-memory computing significantly reduces the matrix multiplication cost of the LSM from $8.28\mu\text{J}$ down to $0.36\mu\text{J}$ as demonstrated in the left panel.

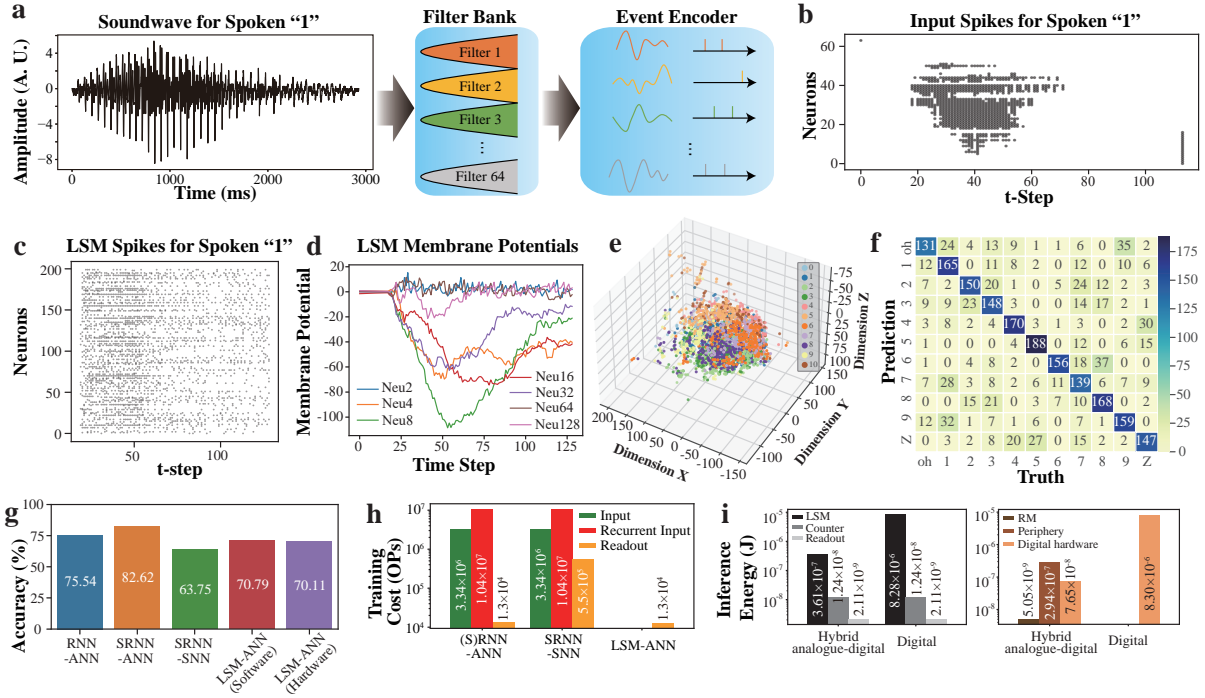


Figure 3. Event-based audio classification with the N-TIDIGITS dataset. **a**, Schematic representation of the event-based audio data capture process using a dynamic audio sensor, comprising a filter bank and an event encoder. **b**, Example of time-binned event data for the spoken digit "1", serving as input to the LSM. **c**, Associated LSM neuron spikes corresponding to the input. **d**, Membrane potentials of selected neurons in response to the input. **e**, 3D distribution of spike number embeddings of the test set, visualized using t-SNE, demonstrating unsupervised clustering. **f**, Confusion matrix characterized by prominent diagonal elements, indicating high classification accuracy. **g**, Accuracy comparison between experimental and simulated model (LSM-ANN), as well as fully trainable counterparts with SNN/ANN encoders/classifiers (RNN-ANN, SRNN-ANN, and SRNN-SNN), exhibiting similar performance. **h**, Breakdown of training complexity. LSM's training complexity is significantly lower than that of SRNN-SNN (by 1,102.92-fold) and SRNN-ANN (by 1,061.60-fold), demonstrating the substantial reduction in training cost by the LSM. **i**, Breakdown of inference energy across various hardware platforms. The estimated inference energy for the digit "7" is approximately 22.07-fold smaller when compared to a fully digital implementation, confirming the enhanced energy efficiency of resistive memory (RM).

Zero-shot Learning Multimodal Event Data

We then develop the zero-shot learning model for multimodal event data by combining resistive memory-based analogue LSM encoders with digital ANN projection layers. The model is trained using contrastive learning for event visual and audio signals. As shown in Fig.4a, for simplicity, the same resistive memory-based LSM encoder receives two input streams: one for N-MNIST images and the other for corresponding N-TIDIGITS audios. The encoded spiking features are accumulated by counters, producing latent vectors of the same dimension. The ANN projection layers are then optimized using contrastive loss. We use images "1" to "7" from N-MNIST and audios "One" to "Seven" from N-TIDIGITS for training. After that, we test the zero-shot transfer capability by querying the model with unseen audios ("Eight" and "Nine") as well as images ("8" and "9") to reveal the generalization capability without finetuning the projection layers. The t-SNE distributions of query samples of both seen and unseen classes after LSM and projection are shown in Fig.4b. The projected features of different classes are distinctively clustered for query samples from both seen and unseen classes. Additionally, the same class is effectively clustered across different modalities, as a result of multimodal contrastive learning.

Fig.4c presents the accuracy of audio-search-image for both query samples of unseen ("8" and "9") and seen classes ("1" through "7") (refer to Table 3-4 in Supplementary Information for details of the dataset). The LSM-ANN model, which does not receive additional training, achieves similar performance as the SRNN-based fully trainable model. Specifically, although the LSM-ANN model has lower accuracy than the fully trainable model on the training task ("1" through "7"), it achieves a zero-shot transfer classification accuracy 88% (87.5%) in simulation (experiment), which is parallel to that of the trainable SRNN-based CLIP and Prototypical networks (see Fig.10 in Supplementary Information for details on training the Prototypical network). The zero-shot transfer performance of the LSM-ANN is also corroborated by the dominant diagonal elements of the

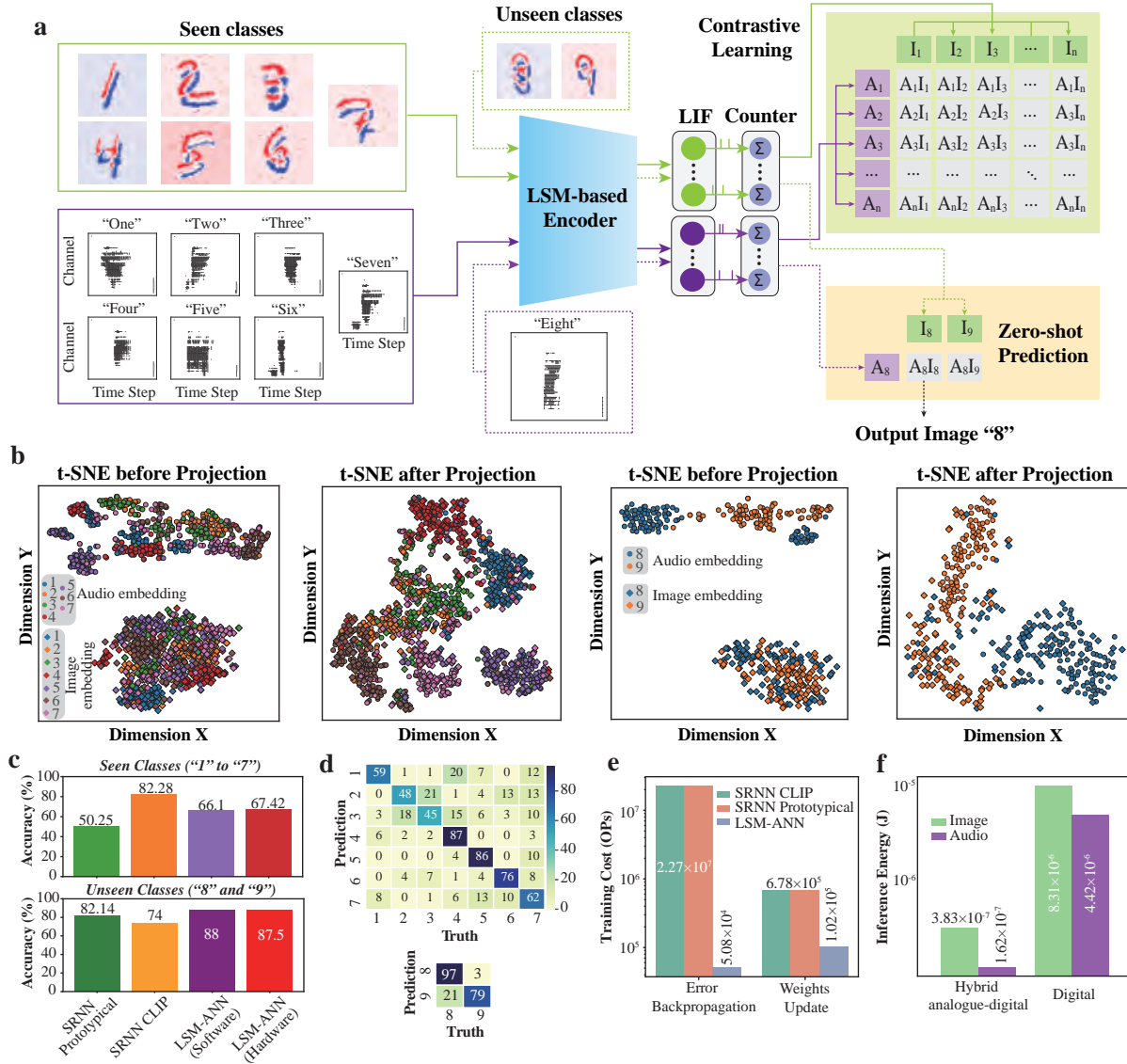


Figure 4. Zero-shot transfer learning of multimodal event data. **a**, Zero-shot transfer learning event visual and audio data with the LSM-ANN using contrastive loss. The model is trained on event images "1" to "7" from the N-MNIST dataset and audios "one" to "seven" from the N-TIDIGITS dataset. The queries of unseen classes encompass images "8" and "9" from N-MNIST as well as audios "eight" and "nine" from N-TIDIGITS. **b**, Distribution of projected query samples from both seen and unseen classes using t-SNE, where same classes of different modalities are clearly aligned while different classes are distinguishable. **c**, Comparison of zero-shot classification accuracy, the LSM-ANN model attains comparable accuracy to state-of-the-art SRNN-based CLIP and Prototypical networks. **d**, Confusion matrix of query samples of seen ("1" to "7") and unseen classes ("8" and "9"). **e**, Training cost breakdown of different zero-shot transfer models. The LSM-ANN model features 152.83-fold reduction of training complexity compared to SRNN-based CLIP and Prototypical networks. **f**, Inference energy of different hardware platforms. The hybrid analogue-digital system shows 23.34-fold improvement over state-of-the-art fully digital implementation (see Table 8 in Supplementary Information for details).

confusion matrix, as shown in Fig.4d. Fig.4e showcases the training costs for SRNN-based CLIP and Prototypical networks, which require approximately 22.7 million and 0.678 million MAC operations, respectively. In comparison, our co-design demonstrates a remarkable 152.83-fold reduction of training complexity, thanks to the fixed random weights of LSM and efficient SNN-ANN interface. Fig.4f showcases the inference energy of the LSM-ANN model when processing a single event image and audio sample. In contrast to digital computers, the inference energy on the projected hybrid analogue-digital platform is $0.545 \mu\text{J}$ ($0.383 \mu\text{J}$ and $0.162 \mu\text{J}$ for image and audio inputs, respectively), resulting in a 23.34-fold enhancement in energy

efficiency thanks to the resistive in-memory computing.

Discussion

In summary, we demonstrate a hardware-software co-design for the sparse and asynchronous event data learning on supervised and zero-shot transfer tasks. Hardware-wise, the stochasticity of resistive switching is leveraged to produce low-cost and scalable random resistive memory that physically implements the weights of an LSM, featuring in-memory computing with large parallelism and high efficiency that overcomes the von Neumann bottleneck and slowdown of Moore’s law. This is augmented by digital hardware for precise and fast ANN weight tuning. Software-wise, contrastive learning with LSM-ANN model not only takes advantage of the physical random projections enabled by random resistive memory arrays in performing multimodal event data embedding, but also substantially reduces the training difficulty thanks to the simple ANN projections in implementing zero-shot transfer learning by generalizing existing knowledge.

Methods

Fabrication of Resistive Memory Chips

The fabricated resistive memory array has a 1T1R structure using the 40nm technology node. Each resistive memory cell is built between the metal 4 and metal 5 layers of the backend-of-line process, consisting of bottom and top electrodes (BE and TE) with a transition-metal oxide dielectric layer. The via of BE is patterned by photolithography and etching, filling with TaN by physical vapor deposition. Above the polished BE via is a 10nm TaN buffer layer. Afterward, a 5nm Ta is deposited and oxidized to form an 8nm TaOx dielectric layer. Finally, the 3nm Ta and 40nm TiN are sequentially deposited by physical vapor deposition to form the TE. After fabrication, the remaining interconnection metals are deposited using the standard logic process. The cells in the same row share BE connections, while those in the same column share TE connections, comprising a 512×512 crossbar array. After 30 minutes of post-annealing at 400 °C in a vacuum environment, the 40nm resistive memory chip shows a high yield and strong endurance performance.

The Hybrid Analogue–Digital Computing System

The hybrid analogue-digital computing system integrates a 40nm resistive memory computing-in-memory chip and a Xilinx ZYNQ system-on-chip (SoC) on a printed circuit board (PCB). For signal inputs, the system offers parallel 64-way analogue voltages generated via an 8-channel digital-to-analog converter (DAC80508, TEXAS INSTRUMENTS, 16-bit resolution), ranging from 0 V to 5 V. For signal collection, the convergence current will be converted to voltages by trans-impedance amplifiers (OPA4322-Q1, TEXAS INSTRUMENTS) and read out by an analog-to-digital converter (ADS8324, TEXAS INSTRUMENTS, 14-bit resolution). Both the analogue and digital conversions are integrated onboard. When performing vector-matrix multiplications, a DC voltage is applied to bit lines of the resistive memory chip through a 4-channel analogue multiplexer (CD4051B, TEXAS INSTRUMENTS) with an 8-bit shift register (SN74HC595, TEXAS INSTRUMENTS). The multiplication result carried by the current from the source line is converted to voltages and passed to the Xilinx SoC for later processing.

LSM-based Supervised Classification

The crossbar array is logically partitioned into two groups conductance matrices (see Fig.2 in Supplementary Information for details), which are employed for N-MNIST and N-TIDIGITS recognition and share the same resistive memory array area. Each group of conductances can be divided into two matrices, $G_I \in \mathbb{R}^{h \times U}$ and $G_R \in \mathbb{R}^{h \times h}$, where U and h denote the dimension of the input feature vector and the number of recurrent neurons, respectively. Specifically, $U = 256$ for N-MNIST, $U = 64$ for N-TIDIGITS, and $h = 200$ for both datasets. Conductances G_I and G_R are used to implement the weight values of the input weights W_I and the recurrent weights W_R of the LSM in Eq. (1). As depicted in Fig.1, the model comprises an LSM backbone and an ANN readout head. LSM is a spiking variant of recurrent neural networks with random weights, first proposed by Maass *et al*⁵⁰. LSMs combined with biologically plausible LIF neurons have demonstrated state-of-the-art performance in addressing vision, audio, and control problems^{57–60}.

LSM Backbone

The LSM consists of an input layer and a recurrent layer to extract spiking features from raw event inputs using fixed and random synaptic weights. This is achieved experimentally by utilizing the random conductance values of the resistive memory.

At time t , the incoming synaptic current I to the i -th recurrent neuron is the weighted summation of the U input spikes θ_α and the h recurrent input spikes θ_β ,

$$I_i(t) = \sum_{\alpha=1}^U w_{(\alpha,i)} * \theta_\alpha(t) + \sum_{\beta=1}^h w_{(\beta,i)} * \theta_\beta(t), \quad (1)$$

where $w_{(\alpha,i)}$ and $w_{(\beta,i)}$ are the randomly initialized synapses connecting the i -th recurrent neuron with the α -th input channel and the β -th recurrent neuron. These synapses remain fixed during training. According to the LIF neuron model, the dynamics of the membrane potential follows,

$$\frac{du(t)}{dt} = \frac{u_{rest} - u(t)}{\tau_{mem}} + \frac{I(t)}{c_{mem}}, \quad (2)$$

where τ_m , c_m , and u_{rest} are constants representing the membrane's leaky time, capacitance, and resting potential, respectively. Once the membrane potential of the i -th recurrent neuron exceeds the firing threshold u_{th} , the neuron generates an action potential $\theta_i(t)$,

$$\theta_i(t) = \begin{cases} 1 & \text{if } u(t) \geq u_{th} \\ 0 & \text{otherwise} \end{cases}. \quad (3)$$

Counter and ANN Readout Map

The counter accumulates asynchronous spiking features and produces a synchronous signal o_i for the i -th neuron over a time window T ,

$$o_i = \sum_{t=1}^{t=T} \theta_i(t). \quad (4)$$

The ANN readout map receives the accumulated neural action potentials from counters and infers labels at a predefined time. Structurally, the readout map is a simple classifier, typically comprising a fully connected layer. In contrast to the SNN part, the weights and biases of the ANN layer are optimized using gradient descent. The functions of the LIF neuron and the ANN readout map are implemented on a computer. All hyperparameters (e.g., firing threshold, decay, time window) are optimized by grid searching the hyperparameter space to maximize hardware performance (see Fig.4 and Fig.5 in Supplementary Information for hyperparameter analysis).

LSM-based Contrastive Learning for Zero-Shot Transfer Learning on Multimodal Event Data

Contrastive learning utilizes a shared LSM structure for both N-MNIST and N-TIDIGITS datasets, with input node sizes u set to 256 and 64, respectively, and a recurrent feature size h of 200. Features are processed through LIF neurons with various hyperparameters and subsequently mapped to the contrastive learning space using a single-layer ANN-type projection layer. The projection dimension size is configured to 64, as depicted in Fig.4.

The LSM structure implementation relies on a shared resistive memory array, while the projection layer function is executed on a commercial digital hardware. The projection layer parameters are updated by the contrastive loss. Specifically, a minibatch of N pairs of vision and audio inputs is randomly sampled. This establishes the contrastive prediction task on LSM encoder pairs of vision features \mathbf{z}_v and audio features \mathbf{z}_a , resulting in pairwise similarities,

$$s_{v,a} = \frac{\mathbf{z}_v^T \mathbf{z}_a}{\|\mathbf{z}_v\| \|\mathbf{z}_a\|}, \quad (5)$$

where $v \in \{1, \dots, N\}$ and $a \in \{1, \dots, N\}$ are indices of projected vision and audio features. The contrastive loss L_c can be defined as,

$$L_c = \frac{1}{2} (\sum_{v=1}^N t_v \log(p_{v,a}) + \sum_{a=1}^N t_a \log(p_{a,v})), \quad (6)$$

where $p_{v,a}$ ($p_{a,v}$) denotes the probabilities of $s_{v,a}$ ($s_{a,v}$) after the softmax function, and t_v (t_a) represents the target label term for vision (audio) embedding. For the target label t_v of the vision feature, mathematically,

$$t_v = \{1, 2, \dots, N\}. \quad (7)$$

The target label t_a of the audio feature operates similarly to that of the vision feature.

Acknowledgement

This research is supported by the National Key R&D Program of China (Grant No. 2018YFA0701500), the National Natural Science Foundation of China (Grant Nos. 62122004, 61874138, 61888102, 61821091), the Strategic Priority Research Program of the Chinese Academy of Sciences (Grant No. XDB44000000), Hong Kong Research Grant Council (Grant Nos. 27206321, 17205922), the Innovation and Technology Commission of Hong Kong (Grant. No. MHP/066/20). This research is also partially supported by ACCESS – AI Chip Center for Emerging Smart Systems, sponsored by Innovation and Technology Fund (ITF), Hong Kong SAR.

Competing Interests

The authors declare no competing interests.

References

1. Liu, K. *et al.* An optoelectronic synapse based on α -in2se3 with controllable temporal dynamics for multimode and multiscale reservoir computing. *Nat. Electron.* **5**, 761–773 (2022).
2. Bartolozzi, C., Indiveri, G. & Donati, E. Embodied neuromorphic intelligence. *Nat. communications* **13**, 1024 (2022).
3. Christensen, D. V. *et al.* 2022 roadmap on neuromorphic computing and engineering. *Neuromorphic Comput. Eng.* **2**, 022501 (2022).
4. Marković, D., Mizrahi, A., Querlioz, D. & Grollier, J. Physics for neuromorphic computing. *Nat. Rev. Phys.* **2**, 499–510 (2020).
5. Lichtsteiner, P., Posch, C. & Delbruck, T. A 128×128 120 db $15 \mu\text{s}$ latency asynchronous temporal contrast vision sensor. *IEEE journal solid-state circuits* **43**, 566–576 (2008).
6. Liu, S.-C., van Schaik, A., Minch, B. A. & Delbruck, T. Asynchronous binaural spatial audition sensor with $2 \times 64 \times 4$ channel output. *IEEE Transactions on Biomed. Circuits Syst.* **8**, 453–464, DOI: [10.1109/TBCAS.2013.2281834](https://doi.org/10.1109/TBCAS.2013.2281834) (2014).
7. Jiménez-Fernández, A. *et al.* A binaural neuromorphic auditory sensor for fpga: a spike signal processing approach. *IEEE transactions on neural networks learning systems* **28**, 804–818 (2016).
8. Choo, K. D. *et al.* Energy-efficient motion-triggered iot cmos image sensor with capacitor array-assisted charge-injection sar adc. *IEEE J. Solid-State Circuits* **54**, 2921–2931, DOI: [10.1109/JSSC.2019.2939664](https://doi.org/10.1109/JSSC.2019.2939664) (2019).
9. Finateu, T. *et al.* 5.10 a 1280×720 back-illuminated stacked temporal contrast event-based vision sensor with $4.86 \mu\text{m}$ pixels, 1.066geps readout, programmable event-rate controller and compressive data-formatting pipeline. In *2020 IEEE International Solid-State Circuits Conference - (ISSCC)*, 112–114, DOI: [10.1109/ISSCC19947.2020.9063149](https://doi.org/10.1109/ISSCC19947.2020.9063149) (2020).
10. Hsu, T.-H. *et al.* A 0.8 v multimode vision sensor for motion and saliency detection with ping-pong pwm pixel. *IEEE J. Solid-State Circuits* **56**, 2516–2524, DOI: [10.1109/JSSC.2021.3075746](https://doi.org/10.1109/JSSC.2021.3075746) (2021).
11. Gallego, G. *et al.* Event-based vision: A survey. *IEEE transactions on pattern analysis machine intelligence* **44**, 154–180 (2020).
12. Yang, M., Liu, S.-C. & Delbruck, T. A dynamic vision sensor with 1% temporal contrast sensitivity and in-pixel asynchronous delta modulator for event encoding. *IEEE J. Solid-State Circuits* **50**, 2149–2160 (2015).
13. Liu, S.-C. & Delbruck, T. Neuromorphic sensory systems. *Curr. opinion neurobiology* **20**, 288–295 (2010).
14. Yao, P. *et al.* Fully hardware-implemented memristor convolutional neural network. *Nature* **577**, 641–646 (2020).
15. Ielmini, D. & Wong, H.-S. P. In-memory computing with resistive switching devices. *Nat. electronics* **1**, 333–343 (2018).
16. Wang, X., Chen, Y., Xi, H., Li, H. & Dimitrov, D. Spintronic memristor through spin-torque-induced magnetization motion. *IEEE electron device letters* **30**, 294–297 (2009).
17. Zidan, M. A., Strachan, J. P. & Lu, W. D. The future of electronics based on memristive systems. *Nat. electronics* **1**, 22–29 (2018).
18. Karunaratne, G. *et al.* In-memory hyperdimensional computing. *Nat. Electron.* **3**, 327–337 (2020).
19. Rao, A., Plank, P., Wild, A. & Maass, W. A long short-term memory for ai applications in spike-based neuromorphic hardware. *Nat. Mach. Intell.* **4**, 467–479 (2022).
20. Karunaratne, G. *et al.* Robust high-dimensional memory-augmented neural networks. *Nat. communications* **12**, 2468 (2021).
21. Moon, J. *et al.* Temporal data classification and forecasting using a memristor-based reservoir computing system. *Nat. Electron.* **2**, 480–487 (2019).
22. Du, C. *et al.* Reservoir computing using dynamic memristors for temporal information processing. *Nat. communications* **8**, 2204 (2017).
23. Sangwan, V. K. & Hersam, M. C. Neuromorphic nanoelectronic materials. *Nat. nanotechnology* **15**, 517–528 (2020).
24. Yu, S. Neuro-inspired computing with emerging nonvolatile memories. *Proc. IEEE* **106**, 260–285 (2018).

25. Chen, X., Han, Y. & Wang, Y. Communication lower bound in convolution accelerators. In *2020 IEEE International Symposium on High Performance Computer Architecture (HPCA)*, 529–541 (IEEE, 2020).
26. Rao, M. *et al.* Thousands of conductance levels in memristors integrated on cmos. *Nature* **615**, 823–829 (2023).
27. Neftci, E. O., Mostafa, H. & Zenke, F. Surrogate gradient learning in spiking neural networks: Bringing the power of gradient-based optimization to spiking neural networks. *IEEE Signal Process. Mag.* **36**, 51–63 (2019).
28. Rueckauer, B., Lungu, I.-A., Hu, Y., Pfeiffer, M. & Liu, S.-C. Conversion of continuous-valued deep networks to efficient event-driven networks for image classification. *Front. neuroscience* **11**, 682 (2017).
29. Rueckauer, B., Lungu, I.-A., Hu, Y. & Pfeiffer, M. Theory and tools for the conversion of analog to spiking convolutional neural networks. *arXiv preprint arXiv:1612.04052* (2016).
30. Wu, Y. *et al.* Direct training for spiking neural networks: Faster, larger, better. In *Proceedings of the AAAI conference on artificial intelligence*, vol. 33, 1311–1318 (2019).
31. Bi, G.-q. & Poo, M.-m. Synaptic modifications in cultured hippocampal neurons: dependence on spike timing, synaptic strength, and postsynaptic cell type. *J. neuroscience* **18**, 10464–10472 (1998).
32. Morrison, A., Diesmann, M. & Gerstner, W. Phenomenological models of synaptic plasticity based on spike timing. *Biol. cybernetics* **98**, 459–478 (2008).
33. Brown, T. *et al.* Language models are few-shot learners. *Adv. neural information processing systems* **33**, 1877–1901 (2020).
34. Dosovitskiy, A. *et al.* An image is worth 16x16 words: Transformers for image recognition at scale. *ICLR* (2021).
35. Alibart, F., Zamanidoost, E. & Strukov, D. B. Pattern classification by memristive crossbar circuits using ex situ and in situ training. *Nat. communications* **4**, 2072 (2013).
36. Prezioso, M. *et al.* Training and operation of an integrated neuromorphic network based on metal-oxide memristors. *Nature* **521**, 61–64 (2015).
37. Yu, S. *et al.* Binary neural network with 16 mb rram macro chip for classification and online training. In *2016 IEEE International Electron Devices Meeting (IEDM)*, 16–2 (IEEE, 2016).
38. Yao, P. *et al.* Face classification using electronic synapses. *Nat. communications* **8**, 15199 (2017).
39. Sheridan, P. M. *et al.* Sparse coding with memristor networks. *Nat. nanotechnology* **12**, 784–789 (2017).
40. Bayat, F. M. *et al.* Implementation of multilayer perceptron network with highly uniform passive memristive crossbar circuits. *Nat. communications* **9**, 2331 (2018).
41. Hu, M. *et al.* Memristor-based analog computation and neural network classification with a dot product engine. *Adv. materials (Deerfield Beach, Fla.)* **30** (2018).
42. Cai, F. *et al.* A fully integrated reprogrammable memristor–cmos system for efficient multiply–accumulate operations. *Nat. Electron.* **2**, 290–299 (2019).
43. Duan, Q. *et al.* Spiking neurons with spatiotemporal dynamics and gain modulation for monolithically integrated memristive neural networks. *Nat. communications* **11**, 3399 (2020).
44. Joshi, V. *et al.* Accurate deep neural network inference using computational phase-change memory. *Nat. communications* **11**, 2473 (2020).
45. Xue, C.-X. *et al.* A cmos-integrated compute-in-memory macro based on resistive random-access memory for ai edge devices. *Nat. Electron.* **4**, 81–90 (2021).
46. Liu, Z. *et al.* Neural signal analysis with memristor arrays towards high-efficiency brain–machine interfaces. *Nat. communications* **11**, 4234 (2020).
47. Zhong, Y. *et al.* Dynamic memristor-based reservoir computing for high-efficiency temporal signal processing. *Nat. communications* **12**, 408 (2021).
48. Milano, G. *et al.* In materia reservoir computing with a fully memristive architecture based on self-organizing nanowire networks. *Nat. Mater.* **21**, 195–202 (2022).
49. Dalgaty, T. *et al.* In situ learning using intrinsic memristor variability via markov chain monte carlo sampling. *Nat. Electron.* **4**, 151–161 (2021).
50. Maass, W., Natschläger, T. & Markram, H. Real-time computing without stable states: A new framework for neural computation based on perturbations. *Neural computation* **14**, 2531–2560 (2002).

51. Radford, A. *et al.* Learning transferable visual models from natural language supervision. In *International conference on machine learning*, 8748–8763 (PMLR, 2021).
52. Orchard, G., Jayawant, A., Cohen, G. K. & Thakor, N. Converting static image datasets to spiking neuromorphic datasets using saccades. *Front. neuroscience* **9**, 437 (2015).
53. Anumula, J., Neil, D., Delbruck, T. & Liu, S.-C. Feature representations for neuromorphic audio spike streams. *Front. neuroscience* **12**, 23 (2018).
54. Snell, J., Swersky, K. & Zemel, R. Prototypical networks for few-shot learning. *Adv. neural information processing systems* **30** (2017).
55. Abbott, L. F. Lapicque’s introduction of the integrate-and-fire model neuron (1907). *Brain research bulletin* **50**, 303–304 (1999).
56. Jia, C. *et al.* Scaling up visual and vision-language representation learning with noisy text supervision. In *International Conference on Machine Learning*, 4904–4916 (PMLR, 2021).
57. Soares, N. & Kudithipudi, D. Deep liquid state machines with neural plasticity for video activity recognition. *Front. neuroscience* **13**, 686 (2019).
58. Zhang, Y., Li, P., Jin, Y. & Choe, Y. A digital liquid state machine with biologically inspired learning and its application to speech recognition. *IEEE transactions on neural networks learning systems* **26**, 2635–2649 (2015).
59. Ponghiran, W., Srinivasan, G. & Roy, K. Reinforcement learning with low-complexity liquid state machines. *Front. Neurosci.* **13**, 883 (2019).
60. de Azambuja, R., Klein, F. B., Adams, S. V., Stoelen, M. F. & Cangelosi, A. Short-term plasticity in a liquid state machine biomimetic robot arm controller. In *2017 International Joint Conference on Neural Networks (IJCNN)*, 3399–3408 (IEEE, 2017).